energy&fuels

pubs.acs.org/EF Article

Experimental Characterization and Pore-Scale Modeling of Iron Precipitation in Shale Reservoirs by Interacting with Hydraulic Fracturing Fluid

Jiahui You and Kyung Jae Lee*

Cite This: *Energy Fuels* 2022, 36, 12997−13006

Read Online

ACCESS | Metrics & More | Article Recommendations

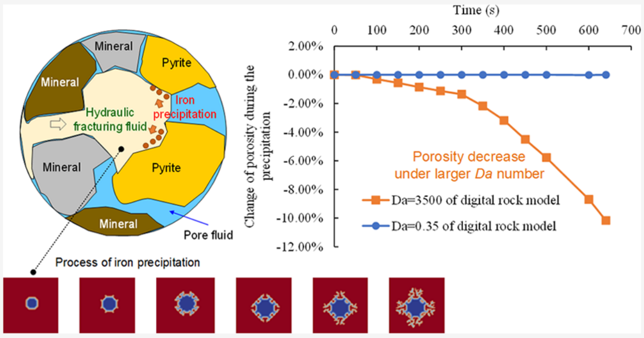

ABSTRACT: It has been reported that ∼60% of total U.S. hydrocarbon production comes from shale reservoirs. Understanding of reactive transport is of fundamental importance to the application in subsurface systems of natural shales that have rich compositions of carbonate, clay, and sulfide, which have high reactivity with water. In this study, we focus on the interaction between pyrite (sulfide) and hydraulic fracturing fluid in shale to investigate the potential impact of iron precipitation on fluid transport. We first conducted the experiments with pyrite samples to calibrate the reaction rate constants for pyrite oxidation (at the pyrite surface) and Fe^{2+} oxidation (in solution). The obtained reaction rate constants were utilized to establish the pore-scale numerical model to track these oxidation reactions. In other words, the reaction rate constants of pyrite surface oxidation and Fe^{2+} oxidation were calibrated by matching the results of numerical simulations with the experimental measurements of ion concentrations. By doing so, we could also obtain confidence in our developed numerical simulator. In numerical simulation case 1, where the reactions of pyrite oxidation and Fe^{2+} oxidation mainly occurred, the transport patterns in the systems were investigated based on the digital rock image model. In numerical simulation case 2, the level-set method was coupled with the reactive transport model to simulate iron(III) hydroxide precipitation on the pyrite surface. The precipitation patterns in the digital rock image model were investigated under different Damköhler numbers (Da_{II}). Under the larger Da_{II}, the precipitated iron(III) hydroxides had a longer dendritic shape, and the precipitation pattern was highly random. The quantified pore-scale parameters obtained from this study are expected to improve continuum-scale models to accurately predict the potential impact of the interaction between pyrite in shale and hydraulic fracturing fluid.

■ INTRODUCTION

It has been known that about 60% of total U.S. hydrocarbon production comes from shale reservoirs.[1] Hydraulic fracturing is widely applied in shale reservoir productions to increase the permeability. Hydraulic fracturing fluid contains diverse chemical additives, such as ethylene glycol, kerosene, guar gum, 2-ethyl hexanol, glycol ether, polyethylene glycol, and hydrochloric acid.[2] When these additives mix with natural fluid in pores, chemical reactions occur, resulting in dissolution and precipitation of various minerals such as the precipitation of iron(III) hydroxide ($Fe(OH)_3$).[3] Such mineral−fluid interactions have critical impacts on the fluid transport, subsequently resulting in porosity−permeability alteration, pore geometry alteration, and flow pathway evolution.

Previous experimental investigation in iron(III) hydroxide precipitation indicated that the released Fe^{2+} oxidation and subsequent Fe^{3+} precipitation were the main paths to iron scale formation in shale reservoirs, where hydraulic fracturing fluid was injected.[3] From that study, it is found that the solution pH was the most important factor affecting the release of Fe into the solution. There are mainly two mechanisms to describe the iron precipitation. When the pH of the solution is around 2.0 in the system, which happens in low carbonate shale formation and around the drill bores, Fe^{2+} is slowly oxidized into Fe^{3+}, and ferrihydrite ($(Fe^{3+})_2O_3{\cdot}0.5H_2O$) is generated in the solution as suspended precipitates. Under the conditions with high carbonate contents and neutral pH, Fe^{2+} is quickly oxidized into Fe^{3+}, and iron precipitates on the pyrite surface.[2] In this work, we mainly focus on iron precipitation on the pyrite surface under the neutral environment because the iron precipitation on the pyrite surface can greatly influence the

Received: August 1, 2022
Revised: September 30, 2022
Published: October 13, 2022

ACS Publications

https://doi.org/10.1021/acs.energyfuels.2c02568

transport pattern. Another previous investigation found that during the injection of hydraulic fracturing fluid, bitumen could be released from shales by interacting with the injected hydraulic fracturing fluid.[4] The liberated bitumen formed a Fe^{3+}—bitumen complex and accelerated the oxidation and precipitation of iron under either neutral or acidic conditions. In the later study, Li et al. quantified the chemical reaction rate for the interaction between hydraulic fracturing fluid and shale matrices.[5] They suggested that the chemical reaction of hydraulic fracturing fluid and shale had a more significant impact in the greater depth zone than the observable reaction zone on the permeability.

Various pore-scale methods were developed to investigate the mineral—fluid interactions, such as the lattice Boltzmann method (LBM) and the direct numerical simulation (DNS) method. In pore scale, tracking the solid—fluid interface in a stable and accurate way is critical for establishing the numerical model: the arbitrary Lagrangian—Eulerian method tracks the zones by moving the mesh on the solid—liquid boundary along the reacting minerals.[6] In the embedded boundary method (EBM), the structured mesh is cut by the irregular shape of the solid—fluid boundary, and the cells over the irregular boundary are refined by the small grids. The small cut cells in the EBM have significant impacts on robustness and stability. The immersed boundary condition (IBC) method takes the advantage of uniform, structured grids, which makes it possible to solve the partial differential equations in a robust and efficient way. In the IBC method, fluid zones are described by irregular configurations in the fixed Eulerian grids, while the solid—fluid interface is represented by mobile Lagrangian grids.[7] The level-set method (LSM) defines the moving velocity to track the evolution of solid—fluid area. Li integrated the LSM with a standard grid-based approach to simulate the acid dissolution and precipitation in complex geometries.[8] In the LBM, the solid—fluid interface is defined as the bounce-back boundary condition, and the volume of the pixel method is used to track the precipitation and dissociation problem.[9,10]

Shale contains various mineral contents, including clay, organic matter, quartz, and calcite. Tight oil is produced from the low-permeability formation that must be hydraulically fractured to improve the permeability, and shale oil is a subset of tight oil.[11] In this work, we mainly focus on shale oil regarding its complex mineral contents with high reactivity. When hydraulic fracturing is conducted, the injected hydraulic fracturing fluid reacts with the minerals in shale such as calcite and pyrite. The chemical reactions may lead to iron precipitation on the pyrite surface and influence the permeability of the shale formation. Given that there has not been a pore-scale numerical investigation aiming to describe the interaction between pyrite and hydraulic fracturing fluid, this study aims to provide the numerical modeling capability in pore scale to quantitatively predict the pore geometry alteration and subsequent fluid transport in such processes. For accurate numerical modeling, we first conducted experiments to provide the reaction rate constants of pyrite oxidation at the surface and Fe^{2+} oxidation in solution. We combined the LSM with the pore-scale reactive transport model to address the pyrite oxidation and Fe^{2+} oxidation under the neutral environment in the first case. The precipitation pattern of iron(III) hydroxide ($Fe(OH)_3$) under the neutral environment was investigated with various Damköhler numbers (Da_{II}) in the second simulation case. The present model is expected to improve the continuum-scale models to accurately predict the potential impact of the interaction between pyrite in shale and hydraulic fracturing fluid. The current model can be applied to the pore-scale simulations using digital rock images with heterogeneous rock structures. From the pore-scale model simulation on the digital rock images, the porosity—permeability relationship can be obtained by dynamically changing the volume and structure of pores due to iron precipitation. These pore-scale results can be used as a valuable input for continuum-scale models for a more realistic description of fluid transport.

METHODOLOGY

Chemical Reaction Paths for Iron Precipitation. As the previous study indicated, Fe^{2+} is expected to be rapidly oxidized into Fe^{3+}, when hydraulic fracturing fluid is injected into shale.[2] Under the neutral environment, $Fe(OH)_3$ and other iron oxides are expected to be generated and precipitated on the pyrite surface. Iron precipitation is influenced by many factors, including the pH value, presence of organic matter (e.g., bitumen), and existing oxides in the hydraulic fracturing fluid, where the relevant reaction mechanisms including reaction kinetics have not been totally understood yet. We focus on the Fe^{3+} precipitation on the pyrite surface, given its substantial impact on the rock morphologies by inducing rough surfaces and subsequent evolution of fluid flow pathways. Here, dissolved oxygen plays a significant role in chemical reactions as can be seen below, and we assumed dissolved oxygen as the only component in water to mimic the hydraulic fracturing fluid in a simplified manner. We considered iron(III) hydroxide ($Fe(OH)_3$) as the precipitating mineral in this work, where the chemical reaction paths are shown as follows[3]

$$\text{pyrite} + H_2O + 3.5O_2\ (aq) \rightarrow 2H^+ + Fe^{2+} + 2SO_4^{2-} \tag{1}$$

$$Fe^{2+} + 0.25O_2\ (aq) + H^+ \rightarrow Fe^{3+} + 0.5H_2O \tag{2}$$

and

$$Fe^{3+} + 3H_2O \rightarrow 3H^+ + Fe(OH)_3 \tag{3}$$

Experimental Methodologies. To provide the reaction kinetics of pyrite surface oxidation (eq 1) and Fe^{2+} oxidation in solution (eq 2) and validate the numerical modeling capability, we conducted the experiment of pure pyrite oxidation in water saturated with oxygen. The reaction kinetics of the last reaction (eq 3, $Fe(OH)_3$ precipitation) were not experimentally measured but were obtained from published data[5] due to its potential error of measurement given the chemical reaction paths.

We first ground a large cubic pyrite into small pieces in the anaerobic environment to prevent surface oxidation. We used a glovebag to grind the cubic pyrite, which was filled with nitrogen. The pyrite sample was put in a 10 mL vial glass bottle with a rubber stopper. We used two pyrite samples, which would be put in the solutions with different pH values: the weight of sample 1 was 0.0841 g and the weight of sample 2 was 0.321 g. We put sample 1 in 10 mL of deionized (DI) water with pH 7 and sample 2 in the 10 mL solution of dilute hydrochloric acid with pH 2. The previous studies showed that the presence of acid will prohibit the surface reaction rate,[2] and hence, we chose a larger sample to obtain more obvious experimental results under an acidic environment. HCl was used because it is one of the most common additives of

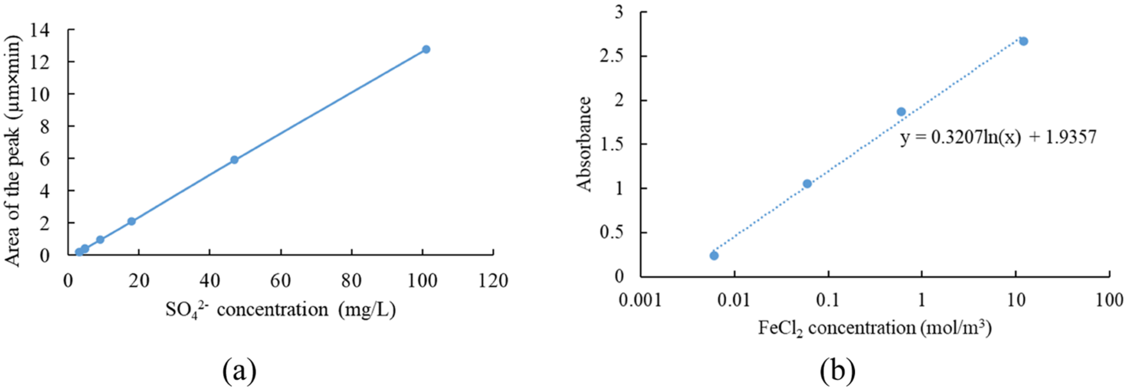

(a) (b)

Figure 1. (a) Calibration of the SO_4^{2-} concentration from ion chromatography. (b) Concentration of standard solutions of $FeCl_2$ and absorbance in UV−vis.

hydraulic fracturing fluid.[2,12,13] The pyrite weight and oxygen concentration were measured before the experiment. The glass bottle was put in a water bath at 80 °C during the reactions. The concentration of the SO_4^{2-} ion was measured using Aquion ion chromatography during the reactions at 0, 4, 10, and 16 days. The Fe^{2+} concentration was measured by UV−vis at 4 and 16 days.

In the ion chromatography analysis, a Dionex AS22-Fast 4 μm analytical column was used to separate the different ions in the solution and measure the conductivity of the ions. $NaHCO_3$ solution was used to elute the system, and the flow rate was set at 1.2 mL/min. We diluted the calibrated standards of the SO_4^{2-} concentration of 2, 4, 10, 20, 50, and 100 mg/L. After the injection of 0.25 μL solution into ion chromatography, we could measure the area of the conductivity peak and obtain the calibrated plot in Figure 1a.

Fe^{2+} concentration was measured by a Nanodrop 2000 UV−vis spectrophotometer. The DI water was the blank solution for the UV−vis background calibration. The micropipette was used to get the 1 μL solution for every measurement. We diluted the $FeCl_2$ standard solution with concentrations of 0.006, 0.06, 0.6, and 12 mol/m^3 to calibrate the concentration of Fe^{2+}. To avoid the oxidation of $FeCl_2$, the solution was diluted in an anaerobic atmosphere. Before adding the DI water into $FeCl_2$, gas sparging was conducted with nitrogen gas to get rid of the dissolved oxygen in the DI water. Then, DI water without oxygen was used to dilute the standard solutions. From the UV−vis spectrophotometer, $FeCl_2$ was in the wavelength of 190 nm.[14] The calibration of $FeCl_2$ is shown in Figure 1b. The x-axis represents the logarithmic value of the solution concentration, and the y-axis represents the absorbance of $FeCl_2$. The logarithmic concentration has a linear relationship with the absorbance. We could calculate the Fe^{2+} concentrations in solution from the absorbance at 190 nm measured from UV−vis.

Development of the Pore-Scale Numerical Model. Pore-scale model is defined as the scale at which each point of space is occupied by a specific phase, either fluid or solid.[6] Here, the whole computational domain is discretized into the structured grids on which the solutions of the mass−balance equation and momentum−balance equation are sequentially computed. In the mass−balance equation, the effects of advection and diffusion were considered to address the ion transport in the porous media. In this way, the spatial distribution of solid and fluid zones can be accurately distinguished.[15] In this study, the pore-scale reactive transport model for iron precipitation was developed based on OpenFOAM, an open-source computational fluid dynamics (CFD) platform.[16] The volume-averaging technique defined the representative elementary volume (REV) with V, the volume of the fluid phase (V_f), and the volume of the solid phase (V_s).

It is found that the size of the REV varies spatially depending on the quantity being represented.[17] If the volume of an element is defined as too large, the continuum variable changes gradually with the volume size. If the volume of an element is defined as too small, the continuum variables exhibit a large fluctuation. The REV is the point that shows the boundary of continuum scale and pore scale. If we are interested in spatial variations in some continuum variables, this transition point represents the target scale at which we wish to measure the fluctuations.[18] The relationship of volume fractions is as follows

$$\varepsilon_s = \frac{V_s}{V},\quad \varepsilon_f = \frac{V_f}{V},\quad \varepsilon_s + \varepsilon_f = 1 \tag{4}$$

The Darcy−Brinkmann−Stokes (DBS) momentum equation was employed to describe the fluid flow[19,20]

$$\frac{1}{\varepsilon_f}\left(\frac{\partial \rho_f \overline{v}_f}{\partial t} + \nabla\cdot\left(\frac{\rho_f}{\varepsilon_f}\overline{v}_f\overline{v}_f\right)\right) = -\nabla\overline{p}_f + \frac{\mu_f}{\varepsilon_f}\nabla^2\overline{v}_f - \mu_f k^{-1}\overline{v}_f \tag{5}$$

where $\overline{v}_f$ is the average velocity, $\overline{p}_f$ is the average pressure, μ_f is the dynamic viscosity, and ρ_f is the fluid density in the system, k is the local permeability and computed by the Kozeny−Carman relationship, $k^{-1} = k_0^{-1}\frac{(1-\varepsilon_f)^2}{\varepsilon_f{}^3}$, and k_0 is the initial local permeability.

The reactive transport was described by the multicomponent advection−diffusion equation[21]

$$\frac{\partial \varepsilon_f C_{f,i}}{\partial t} + \nabla\cdot(u_f C_{f,i}) = \nabla\cdot(\varepsilon_f D_i \nabla C_{f,i}) - a_v R_i(C_{f,i}) \tag{6}$$

where $C_{f,i}$ is the molar concentration of aqueous concentration of species i; D_i is the diffusion coefficient of species i; $R_i(C_{f,i})$ is the reaction rate of species i; a_v is the solid−fluid interface, which is calculated by $a_v = a||\nabla\varepsilon||\psi$ and used to make the reaction rate to be nonzero only at the solid−fluid interface. The evolution of rock geometry was calculated by the mass−balance equation of pyrite

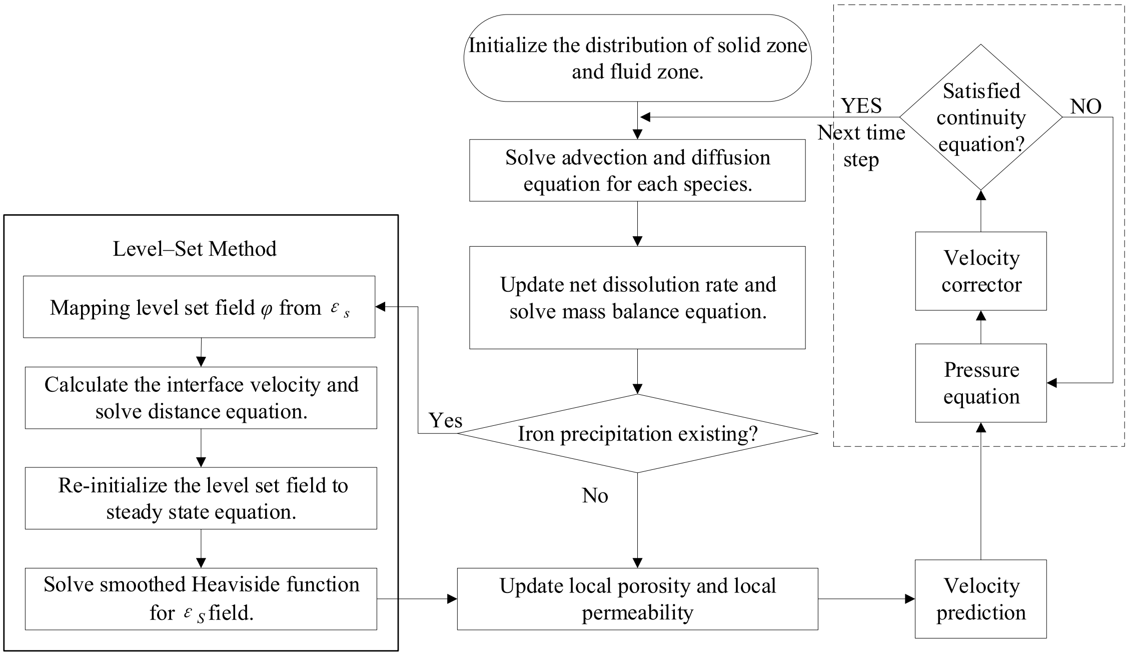

Figure 2. Flow chart of the numerical algorithm of the pore-scale reactive transport model coupled with the LSM.

$$\frac{\partial \varepsilon_s}{\partial t} = a_v R V_m \tag{7}$$

where R is the oxidation rate of pyrite and V_m is the molar volume of pyrite. The right term has a nonzero value on the solid–fluid interface only.

To describe the changing rock–fluid surface by iron precipitation, the level-set method (LSM) was employed, which uses the Eulerian computational techniques to capture the moving interface and shapes.[22] In the LSM, the level-set field (φ) was used to represent the close curvature, Γ. In this study, the level-set field was used to describe the movement of the pyrite surface (Γ) induced by the chemical reaction. The level-set field was generated using the equation

$$\varphi_0 = (2\varepsilon_s - 1)\gamma \tag{8}$$

where $\gamma = 0.75\Delta x$, Δx is the size of mesh cell, and ε_s is the volume fraction of the solid phase. After applying the above equation, the level-set field has the relation

$$\varphi_0 \begin{cases} >0 & \text{in solid phase,} \\ =0 & \text{on the solid} - \text{fluid interface } \Gamma, \\ <0 & \text{in fluid phase} \end{cases} \tag{9}$$

.

The value of φ_0 in the pyrite area is larger than zero; φ_0 in the fluid area is smaller than zero; and φ_0 on the solid–liquid interface is zero. To capture the evolution of the pyrite surface, the evolution of the level-set field is given by the changing rate of φ with respect to time

$$\frac{d\varphi}{dt} = \frac{\partial \varphi}{\partial t} + \vec{u}\cdot\nabla\varphi = 0 \tag{10}$$

where $\vec{u}$ is the surface component of velocity. After projecting the surface component of velocity onto the local unit normal vector, $u_n^\Gamma = \vec{u}\cdot\frac{\nabla\varphi}{|\nabla\varphi|}\Big|_{\varphi=0}$, and the above equation can be written into

$$\frac{\partial \varphi}{\partial t} + u_n^\Gamma|\nabla\varphi| = 0 \tag{11}$$

where $u_n^\Gamma = \frac{K_c k_r C}{\rho_m}$, ρ_m is the molar density of the solid. Solving the above equation leads to numerical oscillation due to the advection of φ with time. By reinitializing the level-set field to the sign function

$$\frac{\partial \varphi}{\partial \tau} - \text{sign}(\varphi^{t+\Delta t})(1 - |\nabla\varphi|) = 0 \tag{12}$$

where τ is artificial time defined as $0.1\Delta x$. The distributions of the solid phase and fluid phase were determined by the smoothed Heaviside function

$$H_\varepsilon(\varphi) = \begin{cases} 0 & \text{if } \varphi < -\in, \\ \frac{1}{2}\left[1 + \frac{\varphi}{\in} - \frac{1}{\pi}\sin(\pi\varphi/\in)\right] & \text{if } |\varphi| \le \in, \\ 1 & \text{if } \varphi > \in \end{cases} \tag{13}$$

, where $\epsilon = 1.5\Delta x$.[22] Then, we can obtain the value of the solid volume fraction for each time step. This LSM method was coupled with the DBS reactive transport method. The numerical solution sequence is shown in Figure 2. For the LSM, we first used eq 8 to assign the level-set field from the volume fraction of the solid. Next, eq 11 was calibrated to obtain the changing closed surface induced by the chemical reactions. After reinitializing the level-set field to the sign function, the volume fraction of the solid could be updated by the smoothed Heaviside function in eq 13.

Calibration of Reaction Rate Constants and Validation of the Numerical Model. To calibrate the reaction rate constants of pyrite oxidation at the surface and Fe^{2+} oxidation in solution and validate our numerical modeling method with the experimental results, we set a 3-D geometric model to replicate the experimental conditions. The 3-D model had 0.019 m length, 0.019 m width, and 0.027 m height, as shown in Figure 3a. From the bottom to 0.01 m in height, we generated the fine mesh to clearly describe the pyrite shape. As shown in Figure 3b, the resolution of this area was 80 (length) × 60 (height) × 80 (width). From 0.01 m to the top of the model, the resolution was 40 (length) × 20 (height) × 40 (width). In the upper area, only the solution reaction (Fe^{2+} oxidation) occurred, and the grid size hardly influenced the accuracy of the simulation. Pyrite sample 1 had a weight of 0.0841 g. The pyrite was initialized as a cubic shape with each side of 0.00256 m by considering the pyrite density of 5 g/cm^3. Sample 2 was initialized as a cubic shape with each side of 0.004 m. We ground the pyrite into small pieces and selected single grain to conduct each case of an experiment. The experimental results of pyrite oxidation are influenced by several factors, such as temperature, oxygen concentration, transport pattern, and reaction rate constant. The fluid−solid interface is one of the factors affecting the experimental results. In the simulation, to begin with the simplified model and find the reaction rate constant, we generated the cubic model to mimic the pyrite piece, as shown in Figure 3c. To estimate the effects of the surface roughness, two different model geometries with the same volumes for the pyrite samples were considered for pH = 7—a cubic model with a smooth surface (Figure 3c) and an irregular model with artificial surface roughness (Figure 3d). Conditions of numerical modeling were set as the same under the experimental conditions. The O_2 concentration was set as 0.256 mol/m^3; the initial pH values of the solution were set at 7 and 2 for sample cases 1 and 2, respectively. The temperature was set at 80 °C under atmospheric pressure. The comparison between the numerical modeling results and the experimental results on the SO_4^{2-} concentration and Fe^{2+} concentration is shown in Figure 4. With the surface roughness, the fluid−solid surface area increased. The generated SO_4^{2-} concentration showed a slightly higher value than the value from the cubic geometry model. We calibrated the reaction rate constant on this geometry model. First, we measured the SO_4^{2-} concentration and Fe^{2+} concentration in solution through experiments. Then, to validate the functionality of the developed numerical model and calibrate the reaction rate constants, we tried to match the SO_4^{2-} concentration and Fe^{2+} concentration in solution computed as the simulation results with the experimentally measured values. To do this, we began with the magnitude of reaction rate constant from the literature as a first guess—input in the numerical simulation. To reproduce the experimental results, we conducted the sensitivity analysis of reaction rate constants of pyrite oxidation and Fe^{2+} oxidation to ion concentrations in solution. We compared several sets of the results under different reaction rate constants and selected the

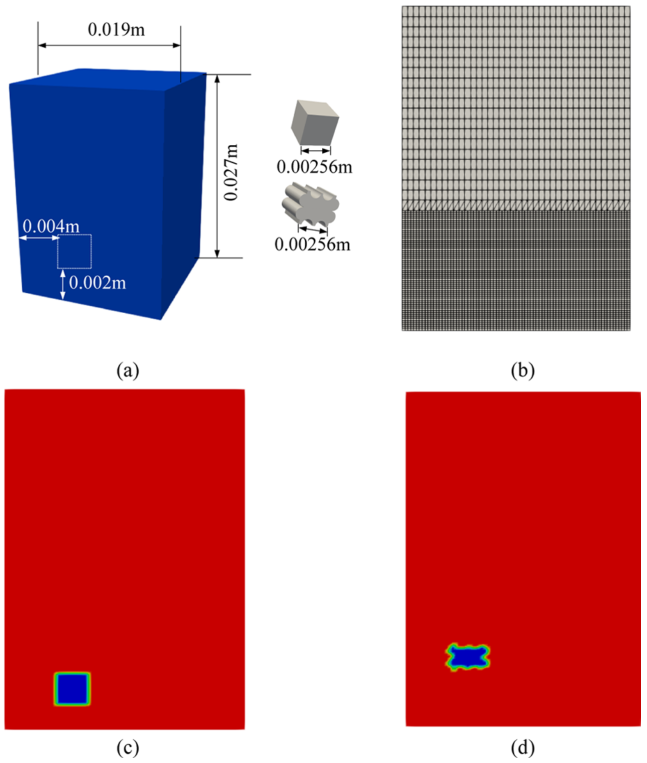

Figure 3. (a) 3-D model to mimic the experiments. (b) Cross section of the mesh. (c) Cross section of the initialization of the smooth cubic model of the pyrite sample. (d) Cross section of the initialization of the irregular shape of the pyrite sample.

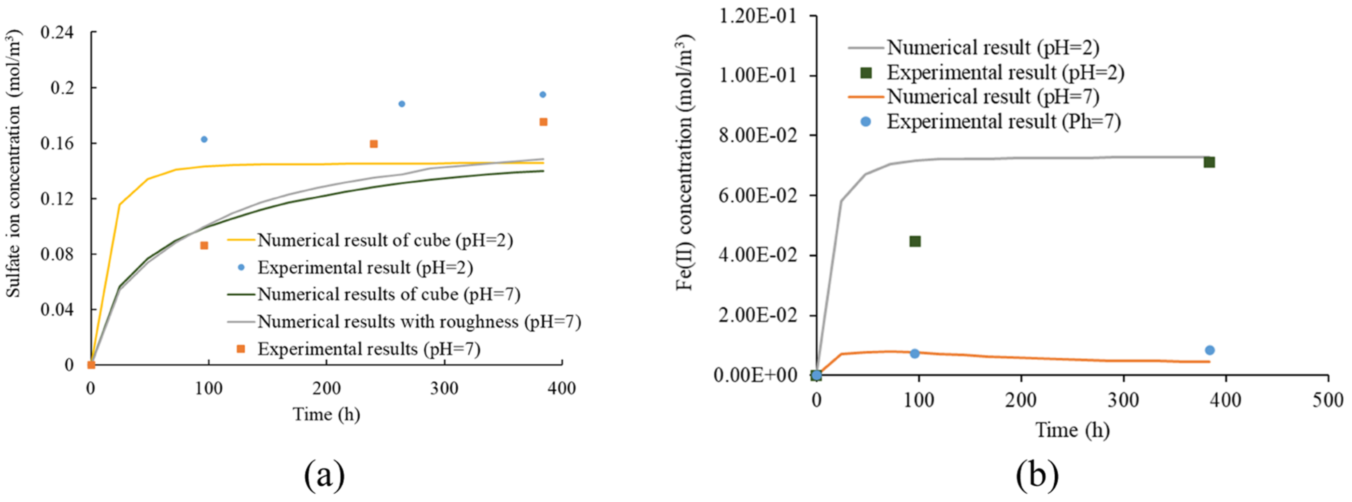

Figure 4. Comparison between experimental results and numerical results of (a) SO_4^{2-} concentration and (b) Fe^{2+} concentration.

currently calibrated reaction rate constants. We could calibrate the reaction rate constants for pyrite oxidation at the surface (eq 1) and Fe^{2+} oxidation in solution (eq 2) as 0.356 mol/m^2 s and 3.06 × 10^{-6} mol/m^3 s, respectively.

■ RESULTS AND DISCUSSION

Problem Setup of Simulation Case 1. In simulation case 1, pyrite surface oxidation (eq 1) and Fe^{2+} oxidation in solution (eq 2) were computationally modeled. Figure 5a shows the scanning electron microscopy (SEM) image (0.37 5mm × 0.424 mm) of calcite within the shale matrix from Barnett shale, and Figure 5b shows the energy-dispersive spectroscopy (EDS) detector image of the elemental map.[23] In the EDS image, the red color indicates quartz and clay, which were assumed to be nonreactive in this problem. The blue color indicates calcite. We assumed that the calcite was consumed after the injection of acid. The yellow color indicates reactive pyrite. According to the above assumptions, the geometric model was developed as shown in Figure 5c, where the red color indicates quartz, and the yellow color indicates pyrite. The generated model mesh is shown in Figure 5d, with a grid resolution of 150 × 170. Because of the nonreactivity of quartz, the mesh was not generated over the quartz area to increase the computational efficiency.

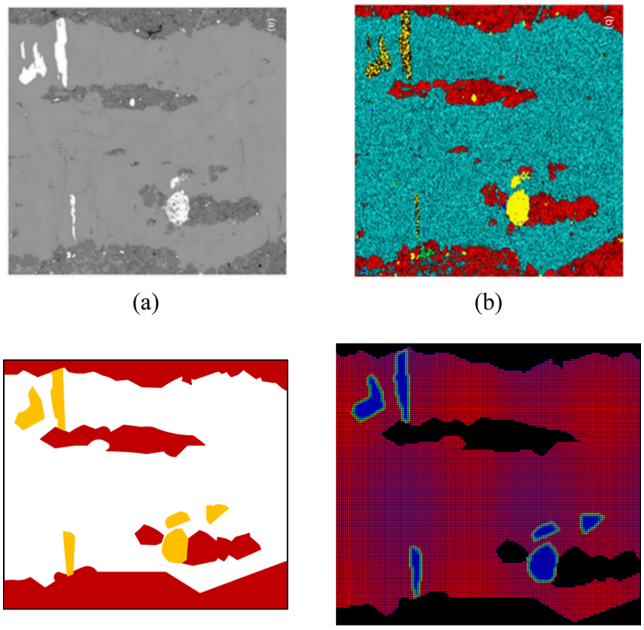
(a) (b)

(c) (d)

Figure 5. (a) SEM image from Barnett shale.[23] (b) EDS image of the composite elemental map.[23] (c) Geometric model of the numerical simulation. (d) Initialization of the pyrite in the computational domain with the mesh.

Table 1 lists the input parameters for pyrite oxidation. At the beginning of the simulation, the fluid area was initialized with the O_2 concentration of 0.256 mol/m^3, where the concentrations of Fe^{2+} and Fe^{3+} were initialized as 0 mol/m^3. The boundary conditions at the inlet (left-hand side) and outlet (right-hand side) for the species were set as zero gradient $\left(\frac{\partial C_i}{\partial n}|_{x=0} = 0\right)$. The pH value was initialized as 7 for the fluid area, and the concentration of H^+ on the inlet boundary was 1 × 10^{-4} mol/m^3.

Table 1. Input Parameters for Simulation Case 1 of Pyrite Surface Oxidation and Fe^{2+} Oxidation in Solution[24]

parameter	symbol	value
fluid density	ρ_l	920 kg·m^{-3}
pyrite density	ρ_s	5000 kg·m^{-3}
fluid viscosity	μ_l	1.0 × 10^{-3} Pa·s
injection velocity	v_{inj}	1.0 × 10^{-5} m·s^{-1}
reaction constant for pyrite surface oxidation (eq 1)	k_{rp}	0.356 mol·m^{-2}·s^{-1}
reaction constant for Fe^{2+} oxidation in solution (eq 2)	$k_{r\text{-iron}}$	3.06 × 10^{-6} mol·m^{-3}·s^{-1}
molecular diffusive coefficient	D_i	5 × 10^{-9} m^2·s^{-1}
inlet O_2 concentration	C_{O_2}	0.256 mol·m^{-3}
equilibrium constant for pyrite surface oxidation (eq 1)	$\log(K_{eq})$	217
equilibrium constant for Fe^{2+} oxidation in solution (eq 2)	$\log(K_{eq})$	0.938

Results of Simulation Case 1. Figure 6 shows the spatial distributions of SO_4^{2-}, Fe^{2+}, and dissolved oxygen (O_2) at t =1000 s. SO_4^{2-} and Fe^{2+} were mainly remaining around the pyrite surface by the pyrite surface oxidation in eq 1. From the geometry of pyrites, it is found that the pyrite surface oxidation (eq 1) and Fe^{2+} oxidation in solution (eq 2) did not result in a significant change in morphology or pore volume. The total concentrations of SO_4^{2-}, Fe^{2+}, and dissolved oxygen in the entire domain are plotted in Figure 7. The concentrations of SO_4^{2-} and Fe^{2+} first sharply increased and gradually reached equilibrium. On the contrary, the concentration of oxygen sharply decreased at the beginning and maintained a relatively constant value.

Problem Setup of Simulation Case 2. In simulation case 2, to investigate the precipitation pattern of iron(III) hydroxide (eq 3) under various conditions, the different values of the second Damköhler number (Da_{II}) were considered, which is defined as follows

$$Da_{II} = \frac{r}{a_v D_A} \tag{14}$$

where r is the reaction rate in m/s, a_v is the volume-averaged effective surface area in 1/m, and D_A is the molecular diffusivity of Fe^{3+} in m^2·s^{-1}. At the inlet boundary on the left-hand side, the Fe^{3+} concentration was set at a constant value of 0.0005 mol/m^3. The volume-averaged effective surface area (a_v) for this pore structure was about 7000 1/m, and the molar volume for pyrite was considered as 23.8 m^3/mol. The Da_{II} numbers were set from 10^{-1} to 10^3. The input parameters are listed in Table 2.

Figure 8 shows the spatial distributions of pore volume fraction with respect to time during the iron(III) hydroxide precipitation. From cases 2-1 to 2-4, we selected the simulation times of 1000, 2000, and 3000 s to be shown. For case 2-5, the times of 200, 400, and 650 s were selected to be shown, considering the high reaction rates. We could observe the different precipitation patterns under different Da_{II} numbers. The pyrite precipitation could be described as dendritic growth, where the growth direction was perpendicular to the solid surface. Under the small Da_{II} (3.5 × 10^{-1}), there was barely precipitation on the pyrite surface. When Da_{II} reached 10^3, the precipitation was formed in a larger dendritic shape in a random manner. Since the precipitation grew along the solid−fluid interface, the surface of the digital rock model became highly heterogeneous. Under a larger Damkohler

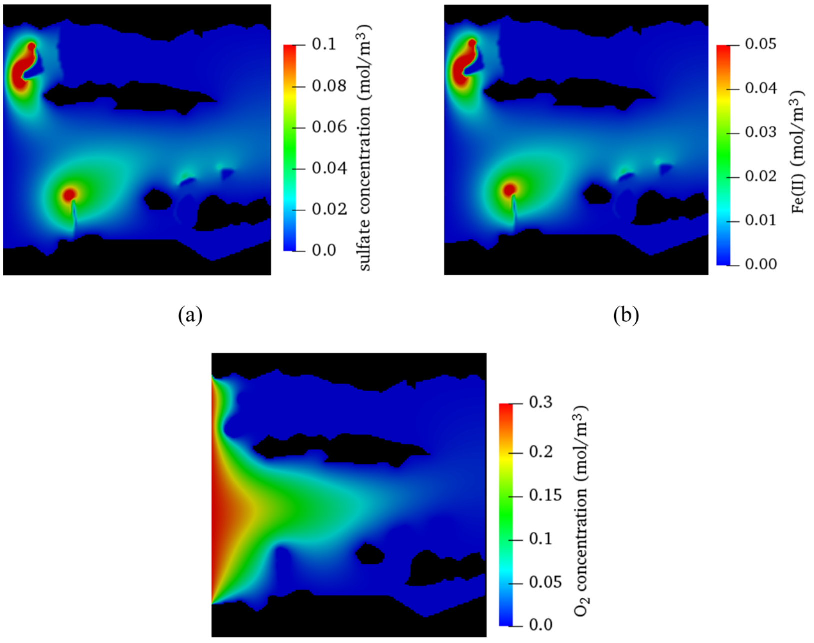

(a)

(b)

(c)

Figure 6. Spatial distribution of species' concentrations at t = 1000 s: (a) SO_4^{2-} concentration, (b) Fe^{2+} concentration, and (c) oxygen concentration.

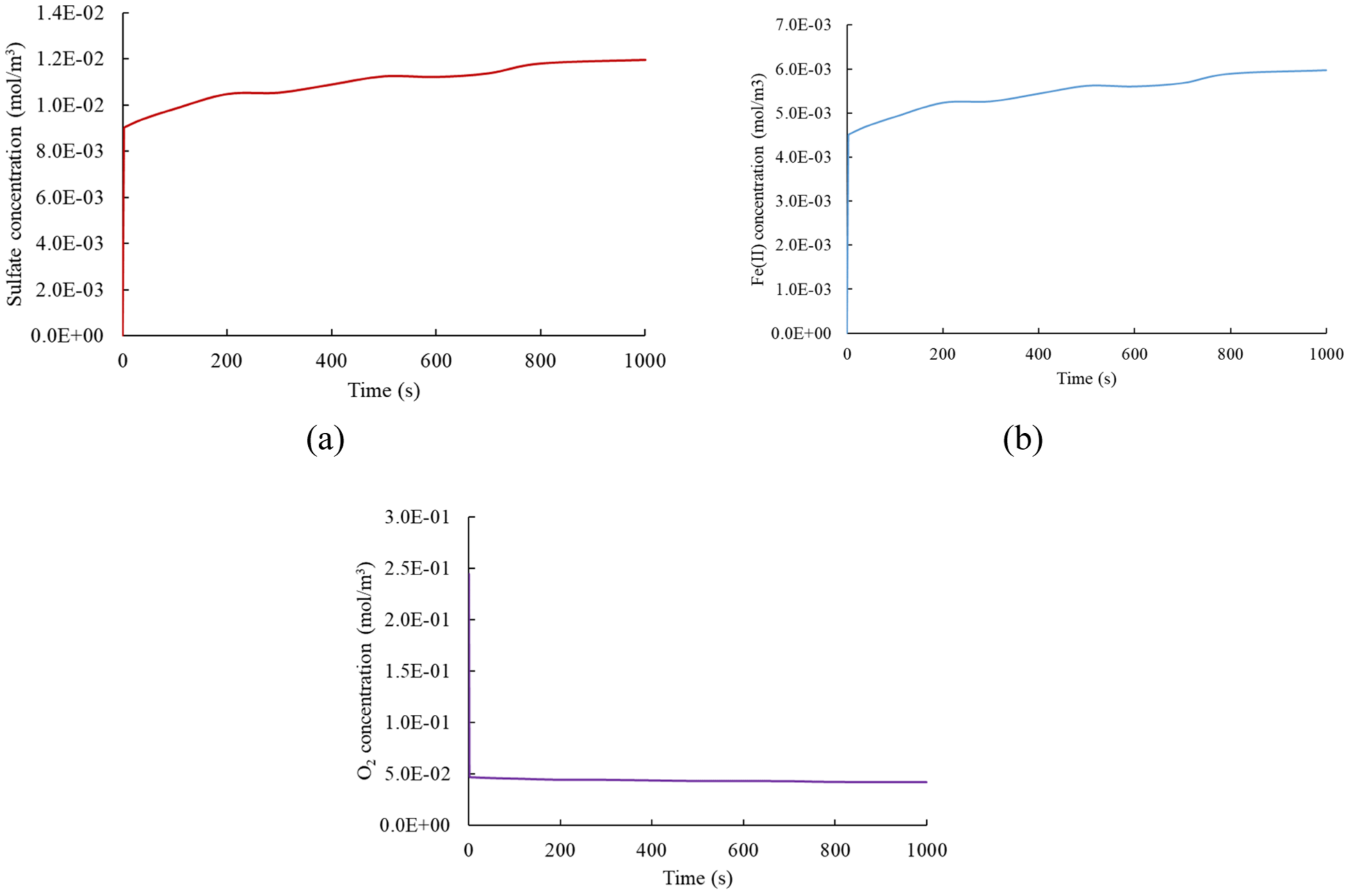

(a)

(b)

(c)

Figure 7. Total concentrations of species in the entire domain: (a) SO_4^{2-} concentration, (b) Fe^{2+} concentration, and (c) oxygen concentration.

Table 2. Input Parameters for the Different Cases of Simulation Case 2

case	Da_{II}	$k_{precipitation}(mol{\cdot}m^{-2}{\cdot}s^{-1})$	$D_i(m^2{\cdot}s^{-1})$
2-1	3×10^0	1×10^{-6}	1×10^{-9}
2-2	3.7×10^1	1×10^{-6}	7.5×10^{-11}
2-3	3.5×10^0	1×10^{-6}	7.5×10^{-10}
2-4	3.5×10^{-1}	1×10^{-8}	7.5×10^{-11}
2-5	3.5×10^3	1×10^{-4}	7.5×10^{-11}

number, the precipitation showed higher heterogeneity. Cases 2-1, 2-2, and 2-3 had the same reaction rate constant but different diffusive coefficients. The growth rate of the precipitation was very similar in these three cases, but the precipitation patterns showed slight differences. By comparing cases 2-1 and 2-2 under the larger Da_{II} with a smaller diffusive coefficient, the precipitation was observed in longer dendritic shapes. This was mainly influenced by the concentration of Fe^{3+} in the field, as shown in Figure 9.

■ CONCLUSIONS

The subsurface formations such as natural shales have a rich composition of sulfide. In such systems, mineral−fluid interactions have critical impacts on the fluid transport, subsequently resulting in pore geometry alteration and flow pathway evolution. In this regard, the present study established the pore-scale reactive transport model to investigate the impacts of mineral (pyrite)−fluid interactions on fluid transport during the injection of hydraulic fracturing fluid into shale. We developed the pore-scale reactive transport model to describe the multispecies transport and chemical reaction paths relevant to iron(III) hydroxide ($Fe(OH)_3$) precipitation. Confidence in the developed numerical simulation method was validated by producing similar ion concentrations obtained with the experimental results. The following specific findings were elucidated: First, the reaction rate constants of pyrite oxidation at the surface and Fe^{2+} oxidation in solution were experimentally measured and calibrated as 0.356 mol/m^2 s and 3.06 × 10^{-6} mol/m^3 s,

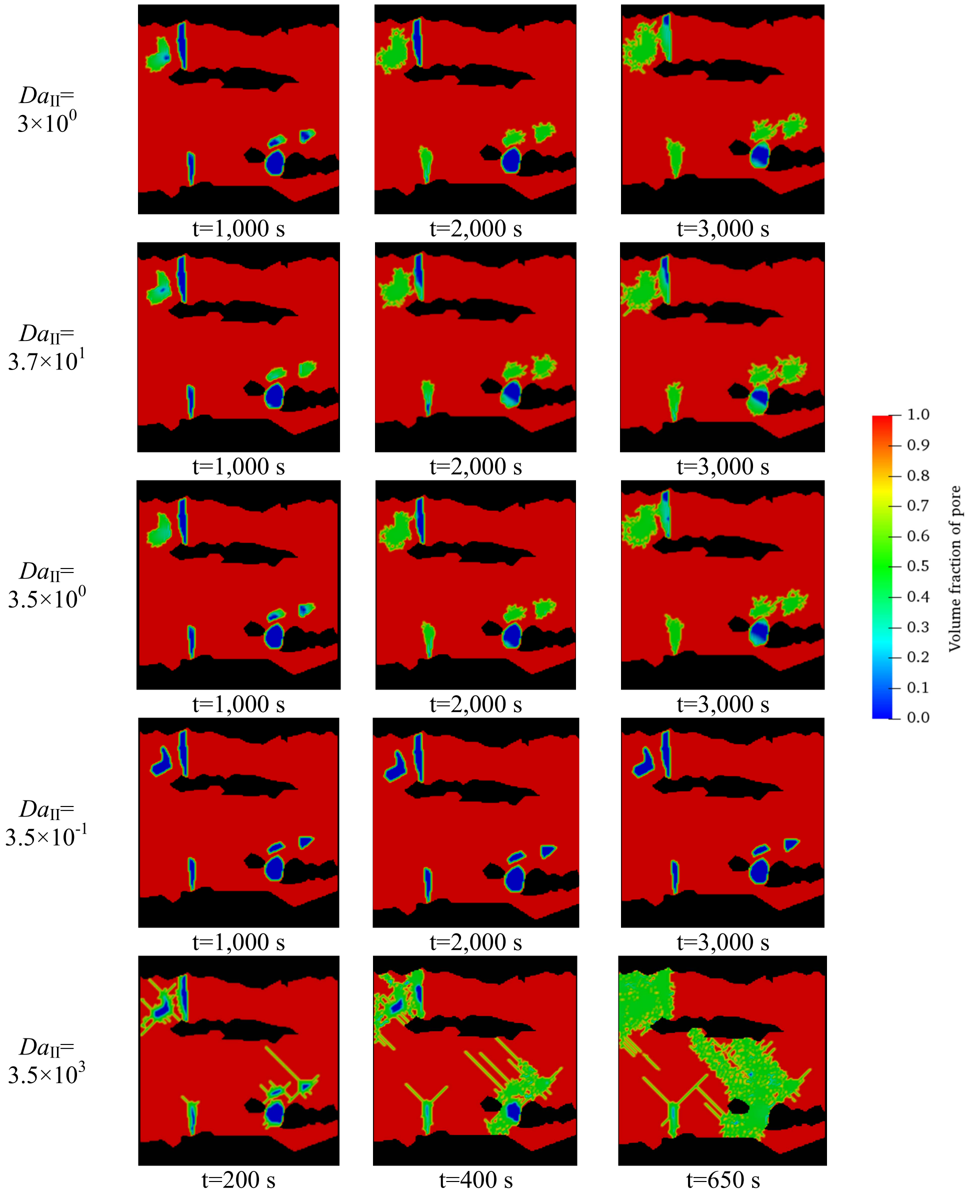

Figure 8. Spatial distributions of the pore volume fraction.

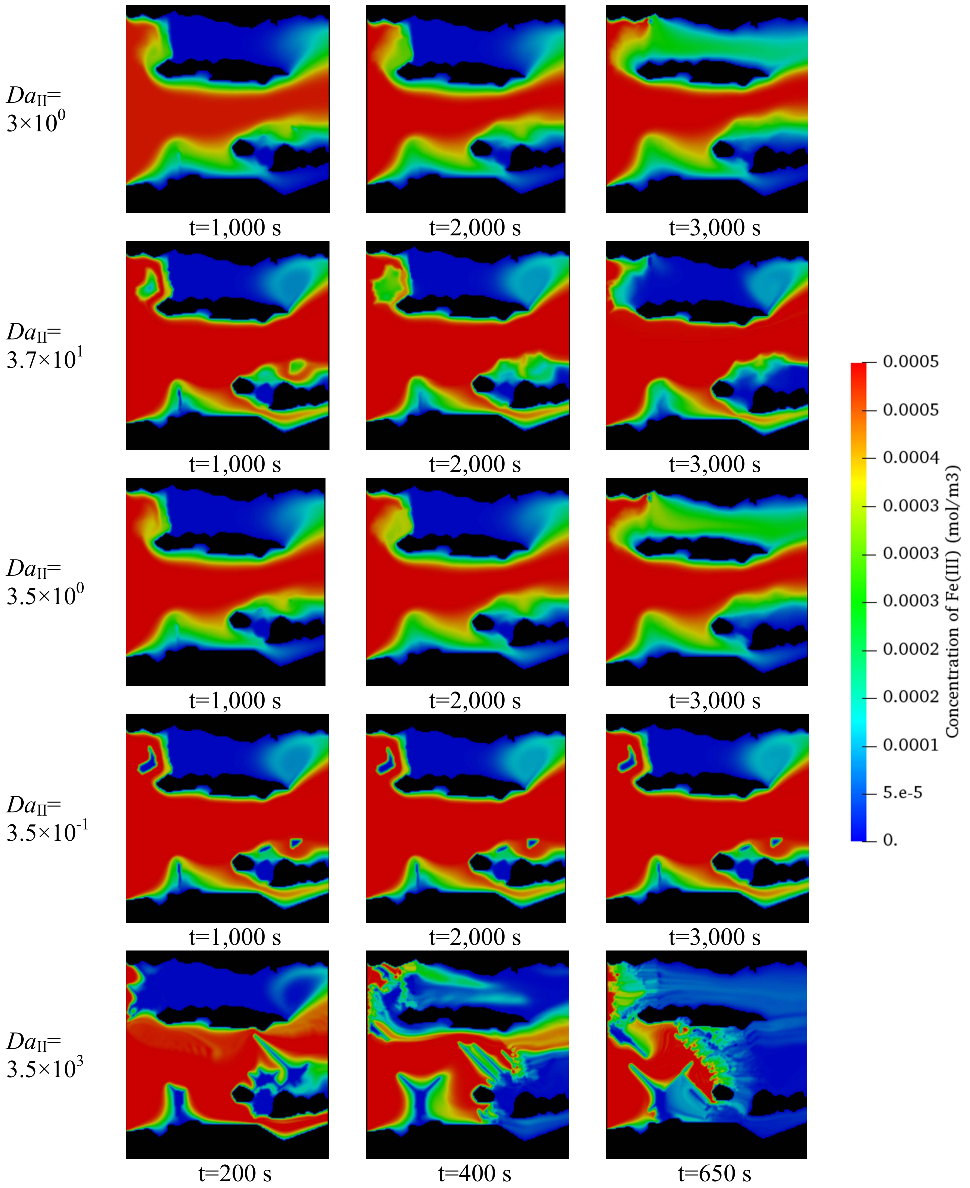

Figure 9. Spatial distributions of Fe^{3+} concentrations.

respectively, through the comparison with the numerical pore-scale modeling. Second, from simulation case 1, it is found that the pyrite surface oxidation and Fe^{2+} oxidation in solution did not result in a significant change in morphology or pore volume. Although the first step of pyrite oxidation does not directly influence the pyrite morphology, the Fe^{3+} precipitation, which is significantly influential on the pyrite morphology, is affected by the preceding reactions. Third, from simulation case 2, there was barely iron(III) hydroxide precipitated on the pyrite surface under small Da_{II}, while the precipitated iron(III) hydroxide had a long dendritic shape in a random manner under higher Da_{II} with a smaller diffusive coefficient. The findings of this pore-scale reactive transport study are expected to improve continuum-scale models to accurately predict the potential impact of the interaction between pyrite in shale and hydraulic fracturing fluid.

■ AUTHOR INFORMATION

Corresponding Author

Kyung Jae Lee − *Department of Petroleum Engineering, University of Houston, Houston, Texas 77204, United States*; orcid.org/0000-0002-5631-9809; Email: kjlee6@central.uh.edu

Author

Jiahui You − *Department of Petroleum Engineering, University of Houston, Houston, Texas 77204, United States*

Complete contact information is available at: https://pubs.acs.org/10.1021/acs.energyfuels.2c02568

Notes

The authors declare no competing financial interest.

■ ACKNOWLEDGMENTS

The authors appreciate the funding for this research from the National Science Foundation under Award 2042504 (CA-

REER: Identifying a New Source of Lithium for Sustainable and Renewable Energy Storage).

REFERENCES

(1) Montgomery, S. L.; Jarvie, D. M.; Bowker, K. A.; Pollastro, R. M. Mississippian Barnett Shale, Fort Worth basin, north-central Texas: Gas-shale play with multi−trillion cubic foot potential. *AAPG Bull.* **2005**, *89*, 155−175.

(2) Jew, A. D.; Dustin, M. K.; Harrison, A. L.; Joe-Wong, C. M.; Thomas, D. L.; Maher, K.; Brown, G. E., Jr.; Bargar, J. R. Impact of organics and carbonates on the oxidation and precipitation of iron during hydraulic fracturing of shale. *Energy Fuels* **2017**, *31*, 3643−3658.

(3) Spencer, M.; Garlapalli, R.; Trembly, J. P. Geochemical phenomena between Utica-Point Pleasant shale and hydraulic fracturing fluid. *AIChE J.* **2020**, *66*, No. e16887.

(4) Li, Q.; Jew, A. D.; Cercone, D.; Bargar, J. R.; Brown, G. E., Jr.; Maher, K. In *Geochemical Modeling of Iron (Hydr)oxide Scale Formation During Hydraulic Fracturing Operations*, Unconventional Resources Technology Conference (URTeC); Society of Exploration Geophysicists: Denver, Colorado, 22−24 July, 2019; pp 3863−3876.

(5) Li, Q.; Jew, A. D.; Kohli, A.; Maher, K.; Brown, G. E., Jr.; Bargar, J. R. Thicknesses of chemically altered zones in shale matrices resulting from interactions with hydraulic fracturing fluid. *Energy Fuels* **2019**, *33*, 6878−6889.

(6) Molins, S.; Soulaine, C.; Prasianakis, N. I.; Abbasi, A.; Poncet, P.; Ladd, A. J. C.; Starchenko, V.; Roman, S.; Trebotich, D.; Tchelepi, H. A.; Steefel, C. I. Simulation of mineral dissolution at the pore scale with evolving fluid-solid interfaces: review of approaches and benchmark problem set. *Comput. Geosci.* **2021**, *25*, 1285−1318.

(7) Mittal, R.; Iaccarino, G. Immersed boundary methods. *Annu. Rev. Fluid Mech.* **2005**, *37*, 239−261.

(8) Li, X.; Huang, H.; Meakin, P. Level set simulation of coupled advection-diffusion and pore structure evolution due to mineral precipitation in porous media. *Water Resour. Res.* **2008**, *44*, No. W12407.

(9) Li, Z.; You, J.; Qin, G. In *A Pore-Scale Study on the Shale-Gas Transport with CO2 Injection Applying the Lattice Boltzmann Method*, SPE Improved Oil Recovery Conference, 2022.

(10) Li, Z.; Qin, G. In *Pore-Scale Study of Effects of Hydrate Morphologies on Dissociation Evolutions Using Lattice−Boltzmann Method*, Offshore Technology Conference, 2021.

(11) Pathak, M.Storage Mechanisms of Oil and Gas in Shales. In *Encyclopedia of Petroleum Geoscience*; Sorkhabi, R., Ed.; Springer International Publishing: Cham, 2018; pp 1−6.

(12) Li, N.; Chen, F.; Yu, J.; Han, P.; Kang, J. Pre-acid system for improving the hydraulic fracturing effect in low-permeability tight gas reservoir. *J. Pet. Explor. Prod.* **2021**, *11*, 1761−1780.

(13) Ashena, R.; Aminzadeh, F.; Khoramchehr, A. Production Improvement via Optimization of Hydraulic Acid Fracturing Design Parameters in a Tight Carbonate Reservoir. *Energies* **2022**, *15*, 1947.

(14) Parinayok, P.; Yamashita, M.; Yonezu, K.; Ohashi, H.; Watanabe, K.; Okaue, Y.; Yokoyama, T. Interaction of Au (III) and Pt (IV) complex ions with Fe (II) ions as a scavenging and a reducing agent: A basic study on the recovery of Au and Pt by a chemical method. *J. Colloid Interface Sci.* **2011**, *364*, 272−275.

(15) You, J.; Lee, K. J. Pore-Scale Study to Analyze the Impacts of Porous Media Heterogeneity on Mineral Dissolution and Acid Transport Using Darcy−Brinkmann−Stokes Method. *Transp. Porous Media* **2021**, *137*, 575−602.

(16) Weller, H. G.; Tabor, G.; Jasak, H.; Fureby, C. A tensorial approach to computational continuum mechanics using object-oriented techniques. *Comput. Phys.* **1998**, *12*, 620−631.

(17) Zhang, D.; Zhang, R.; Chen, S.; Soll, W. E. Pore scale study of flow in porous media: Scale dependency, REV, and statistical REV. *Geophys. Res. Lett.* **2000**, *27*, 1195−1198.

(18) White, J. A.; Borja, R. I.; Fredrich, J. T. Calculating the effective permeability of sandstone with multiscale lattice Boltzmann/finite element simulations. *Acta Geotech.* **2006**, *1*, 195−209.

(19) Soulaine, C.; Roman, S.; Kovscek, A.; Tchelepi, H. A. Mineral dissolution and wormholing from a pore-scale perspective. *J. Fluid Mech.* **2017**, *827*, 457−483.

(20) You, J.; Lee, K. J. A pore−scale investigation of surface roughness on the evolution of natural fractures during acid dissolution using DBS method. *J. Pet. Sci. Eng.* **2021**, *204*, No. 108728.

(21) Molins, S.; Trebotich, D.; Steefel, C. I.; Shen, C. An investigation of the effect of pore scale flow on average geochemical reaction rates using direct numerical simulation. *Water Resour. Res.* **2012**, *48*, No. W03527.

(22) Osher, S.; Fedkiw, R.; Piechor, K. Level set methods and dynamic implicit surfaces. *Appl. Mech. Rev.* **2004**, *57*, B15.

(23) Vega, B.; Ross, C. M.; Kovscek, A. R. Imaging-Based Characterization of Calcite-Filled Fractures and Porosity in Shales. *SPE J.* **2015**, *20*, 810−823.

(24) Li, Q.; Jew, A. D.; Brown, G. E., Jr.; Bargar, J. R.; Maher, K. Reactive transport modeling of shale−fluid interactions after imbibition of fracturing fluids. *Energy Fuels* **2020**, *34*, 5511−5523.

https://doi.org/10.1021/acs.energyfuels.2c02568
Energy Fuels 2022, 36, 12997−13006